CHAPTER

20 Fluorescence Lifetime Imaging Microscopy for Quantitative Biological Imaging

Leng-Chun Chen, William R. Lloyd, III, Ching-Wei Chang, Dhruv Sud, and Mary-Ann Mycek

Department of Biomedical Engineering, University of Michigan, Ann Arbor, Michigan, USA

CHAPTER OUTLINE

Methods in Cell Biology, Volume 114 **ISSN 0091-679X**

http://dx.doi.org/10.1016/B978-0-12-407761-4.00020-8

Abstract

Fluorescence lifetime imaging microscopy (FLIM) is a method for measuring fluorophore lifetimes with microscopic spatial resolution, providing a useful tool for cell biologists to detect, visualize, and investigate structure and function of biological systems. In this chapter, we begin by introducing the basic theory of fluorescence lifetime, including the characteristics of fluorophore decay, followed by a discussion of factors affecting fluorescence lifetimes and the potential advantages of fluorescence lifetime as a source of image contrast. Experimental methods for creating lifetime maps, including both time- and frequency-domain experimental approaches, are then introduced. Then, FLIM data analysis methods are discussed, including rapid lifetime determination, multiexponential fitting, Laguerre polynomial fitting, and phasor plot analysis. After, data analysis methods are introduced that improve lifetime precision of FLIM maps based upon optimal virtual gating and total variation denoising. The chapter concludes by highlighting several recent FLIM applications for quantitative biological imaging, including Förster resonance energy transfer-FLIM, fluorescence correlation spectroscopy-FLIM, multispectral-FLIM, and multiphoton-FLIM.

INTRODUCTION TO FLUORESCENCE LIFETIME IMAGING MICROSCOPY

There has been significant growth in the use of fluorescence in the biological sciences during the past few decades (Lloyd, Chen, & Mycek, 2013; Lloyd, Chen, Wilson, & Mycek, 2013). Besides environmental monitoring, clinical chemistry, DNA sequencing, and genetic analysis by fluorescence *in situ* hybridization, fluorescence is used for cell identification and sorting in flow cytometry, and to reveal the localization and movement of intracellular substances in cellular imaging by means of fluorescence microscopy (Lakowicz, 2006).

Microscopic imaging of steady-state fluorescence intensity is routinely employed for studies in cell biology to reveal information regarding cellular morphology, intracellular ion concentrations, protein binding, lipid content, and membrane status (Rudolph & Kempe, 1997). However, intensity-based measurements are vulnerable to artifacts such as variation in excitation source intensity, detector gain setting, optical loss in the optical path and/or sample, variation in sample fluorophore concentration, photobleaching, and microscope focusing. Further, fluorophores with similar excitation and emission spectra may be impossible to differentiate with steady-state fluorescence intensity imaging.

Fluorophore lifetime is the property describing on average how rapidly an excited-state fluorophore decays. Accordingly, fluorescence lifetime imaging microscopy (FLIM) is a technique for producing spatially resolved images of fluorophore lifetime, providing another dimension of information for visualizing fluorophores and an additional source of contrast (Chang & Mycek, 2012b). As an example, and as can be inferred from Table 20.1, flavin adenine dinucleotide (FAD) is

Table 20.1 Endogenous and exogenous fluorophores used in cell biology (ISS; Urayama & Mycek, 2003)

Fluorophore	Solvent	Excitation max [nm]	Emission max [nm]	Life time [ns]
Endogenous				
Tryptophan	Water	295	353	3.1
Tyrosine	Water	275	304	3.6
Phenylalanine	Water	260	282	6.8
NAD(P)H	Water	350	460	0.4
FAD	Water	450	525	4.7
FMN	Water	450	525	2.3
Exogenous				
ATTO 565	Water	561	585	3.4
Rhodamine B	Water	562	583	1.68
Cy3	PBS	548	562	0.3
Cy5	PBS	646	664	1
DAPI	TRIS/ EDTA	341	496	0.16
FITC	PB pH 7.8	494	518	4.1
Fluorescein	PB pH 7.5	495	517	4
GFP	Buffer pH 8	498	516	3.2
Hoechst 33342	TRIS/ EDTA	336	471	0.35
Lucifer Yellow	Water	428	535	5.7

The standard fluorophores have single-exponential decay fluorescence lifetimes. PBS, phosphate-buffered saline, pH 7.4; TRIS/EDTA (1 mM, pH 7.4), tris*(hydroxymethyl)aminomethane/ ethylenediamine-tetraacetic acid; PB, phosphate buffer.*

distinguished from flavin mononucleotide with fluorescence lifetime approaches such as FLIM, as can ATTO 565 from Rhodamine B, despite the fact that their fluorescence spectra overlap. Further, fluorescence lifetime is known to be sensitive to the fluorophore's local environment and can reveal information on pH, oxygenation, temperature, and molecular associations (Lakowicz, 2006; Tadrous, 2000). For example, Fig. 20.1 illustrates the capability of FLIM to study Förster resonance energy transfer (FRET or FLIM-FRET), which reports on molecular associations. Here, FLIM-FRET was employed to monitor the localization of pre-mRNA splicing in a cell nucleus (Ellis et al., 2008). These results showed that spatial mapping with FLIM-FRET revealed differences in splicing factors interactions within complexes located in separate subnuclear domains.

Section 1 begins with the basics of fluorescence lifetime sensing, including the characteristics of fluorophore excited-state decay, a discussion of factors affecting fluorescence lifetimes, and the usefulness of fluorophore lifetimes as a source of contrast. Then, in Section 2, both time-domain (TD) and frequency-domain (FD) approaches to measure fluorescence lifetimes and their associated data analysis methods will be

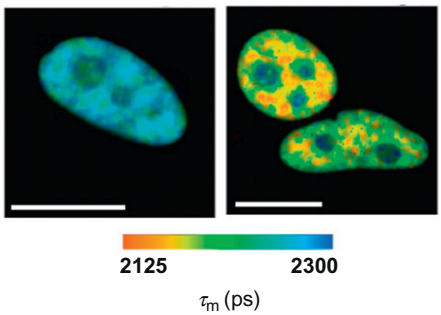

FIGURE 20.1

Intensity-based FRET measurements are limited by the typical assumption that FRET occurs in all observable donor molecules and the resulting complexity of data analysis. Alternatively, FLIM-FRET measurements are not limited by such an assumption. FLIM-FRET measurements can provide robust measurements that depend on the physical fluorescence lifetime and are thus internally calibrated with relatively straightforward data analysis methods. Such quantification is achieved by measuring fluorescence lifetime, which directly relates to the environment and binding state of a fluorescent molecule. Here, FLIM-FRET was employed to monitor nuclear pre-mRNA splicing, a process necessary for the functional coding sequence ligation. Living HeLa cells were monitored with FLIM to map the localization of the interaction between the splicing protein (U1 70K) and a serine/arginine-rich protein (SF2/ASF), which plays a key role in constitutive and alternating splicing. HeLa cells were transfected with EGFP-U1 70K (donor) and cotransfected with either mCherry-C1 or mCherry-SF2/AFS (acceptor). The donor fluorescence lifetime in HeLa cells was measured in the presence of either mCherry-C1 (negative control, left) or mCherry-SF2/AFS (right). Cotransfection of EGFP-U1 70K and mCherry-SF2/AFS resulted in a reduction of the mean donor lifetime, which is indicative of FRET. Scale bar: 10 μm (Ellis, Lleres, Denegri, Lamond, & Caceres, 2008).

described. Various applications of FLIM, ranging from FLIM-FRET, fluorescence correlation spectroscopy-FLIM (FCS-FLIM), multispectral-FLIM (MS-FLIM), and multiphoton-FLIM (MP-FLIM), will be highlighted in Section 3, followed by a Section "Summary".

20.1 FLUOROPHORE EXCITED-STATE LIFETIME: τ

20.1.1 Basic theory

Figure 20.2 is a simplified version of a Jablonski diagram to illustrate the molecular fluorescence process, where S_0 and S_1 are the ground and first excited electronic states, respectively, and the horizontal lines represent different vibrational states of the fluorophore. In condensed phases, after absorption of a photon, almost all excited molecules rapidly relax to the lowest vibrational level of the first excited state, from which they return to the ground state via: nonradiative or radiative decay process. The radiative decay rate Γ depends on the electronic properties of an isolated fluorophore. Molecular

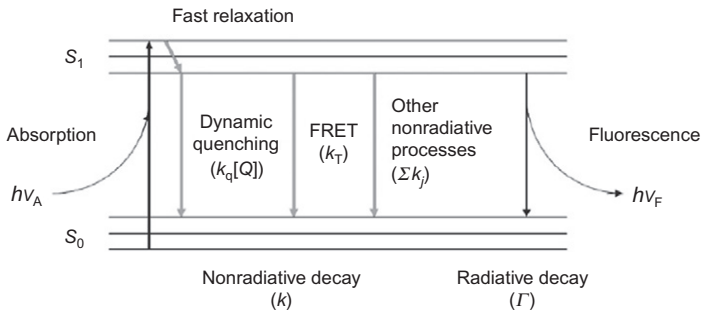

FIGURE 20.2

Simplified Jablonski diagram. k_q, Bimolecular quenching constant; $[Q]$, Quencher concentration (see Section 1.2); k_T, energy transfer rate constant (see Section 3.1); k_j, rate constant for nonradiative processes other than dynamic quenching and FRET (Chang, Sud, & Mycek, 2007).

interactions, such as dynamic (or collisional) quenching (see Section 1.2) and FRET (see Section 3.1), are accounted for in the nonradiative decay rate k.

Radiative decay is responsible for fluorescence emission, which provides detectable photons. However, since both decay processes depopulate fluorescent molecules in the first excited state, with fluorophore population $N(t)$, the overall decay of fluorescence emission intensity, proportional to $N(t)$, is attributed to both decay rates. In the simplest case, fluorescence decay follows the stochastic exponential decay as shown in Eqs. (20.1) and (20.2).

$$\frac{dN(t)}{dt} = -(\Gamma + k)N(t) \tag{20.1}$$

$$N(t) = N_0 e^{-(\Gamma+k)t} = N_0 e^{-t/\tau} \tag{20.2}$$

where N_0 is the initial number of fluorescent molecules in the first excited state, and

$$\tau = \frac{1}{\Gamma + k} \tag{20.3}$$

is the fluorescence lifetime, indicative of the average time a molecule spends in the excited state prior to returning to the ground state. Both nonradiative and radiative decay rates affect the value of τ, as shown in Eq. (20.3). Another important property of fluorophores is the quantum yield Q, defined as the ratio of the number of emitted photons to the number of absorbed photons, which is given by

$$Q = \frac{\Gamma}{\Gamma + k} \tag{20.4}$$

Note that $0 \leq Q \leq 1$ and Q can be close to unity if $k \ll \Gamma$. Generally, higher Q means higher fluorescence efficiency, which is usually favored in fluorescence applications. Commonly employed fluorophores such as tryptophan has a Q of 0.13, Rhodamine B has a Q of 0.31, Cy3 has a Q of 0.04, and fluorescein has a Q of

0.95 (ISS; Urayama & Mycek, 2003). Although Q can be used as a source of contrast, experimental protocols for estimating Q are strict and controlled, making such protocols difficult to apply in biological samples.

20.1.2 Key features of fluorescence lifetime sensing

Fluorescence lifetime is an intrinsic property of a fluorophore and is insensitive to a variety of intensity-based artifacts. Factors such as variations in excitation source intensity, detection gain setting, optical loss in the optical path and/or sample, variation in sample fluorophore concentration, photobleaching, and microscope focusing will all affect measured fluorescence intensities, but will leave the intrinsic excited-state fluorophore lifetime unchanged (Lloyd, Wilson, Chang, Gillispie, & Mycek, 2010). In addition, due to the nature of nonradiative decay processes, fluorescence lifetimes are sensitive to the fluorophore's microenvironment, including factors such as temperature, pH, oxygen concentration, polarity, molecular associations (binding), ion concentration, and relaxation through collisional (dynamic) quenching and FRET. Figure 20.3 is an example of the intensity-independent nature of FLIM measurements; here, the measured fluorescence lifetime, an intrinsic property of the fluorescent molecule, remains unaffected by variations in fluorophore concentration (within limits). As expected, these same variations in fluorophore concentration were shown to directly impact the measured fluorescence intensity.

Fluorescence quenching is generally classified into two primary types: static and dynamic. The concepts of static and dynamic quenching are shown in Fig. 20.4. Static quenching occurs due to the formation of nonfluorescent complexes via the interaction between fluorophores and other molecules in solution known as

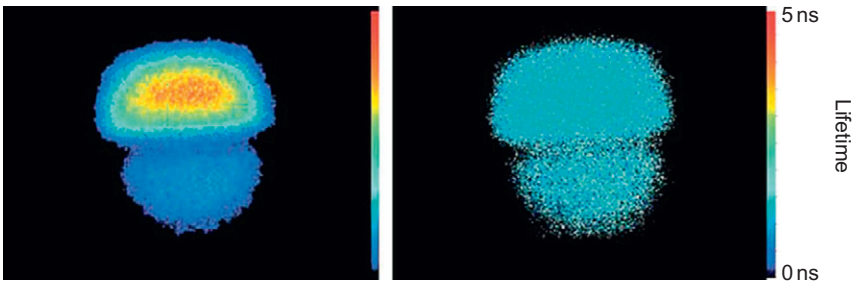

FIGURE 20.3

Intensity-independent fluorophore lifetimes recovered by FLIM. Despite a factor of four difference in POPOP concentration and hence signal intensity (left), the three-gate protocol lifetime map (right) showed identical mean lifetimes for the two POPOP samples. The images were of POPOP in ethanol solutions in two quartz capillaries. The capillary interface was on the diameter, with the circular region as the illumination area. The intensity images were background subtracted before calculation of lifetime map (Urayama et al., 2003).

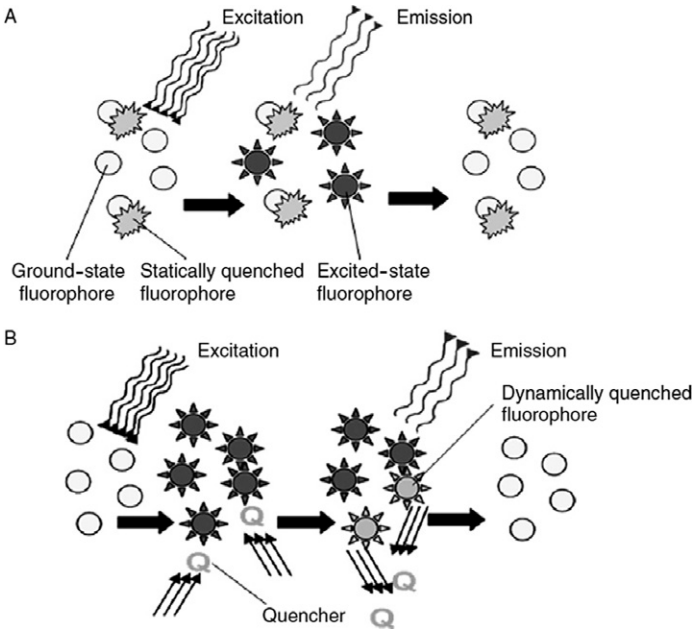

FIGURE 20.4

Static quenching (A) occurs due to the formation of nonfluorescent complexes from the interaction between fluorophores and other molecules in solution known as quenchers. Lifetime imaging is insensitive to static quenching. On the other hand, dynamic quenching (B) happens during the decay process, when excited-state fluorophores are de-excited upon contact with the quenchers. As a result, detected lifetime will be shortened (Chang et al., 2007).

quenchers. Fluorescence lifetime imaging is insensitive to static quenching, as other unbound (hence still fluorescent) fluorophores retain their fluorescent properties. On the other hand, dynamic (or collisional) quenching happens during the fluorescence decay process, when some excited-state fluorophores are de-excited upon contact with the quenchers and follow a nonradiative decay process (see Fig. 20.2), which leads to a faster decay of excited-state fluorophore population and hence a shorter fluorescence lifetime.

Therefore, measuring fluorescence lifetime provides a means of probing the local fluorophore environment. FLIM was reported (Sanders, Draaijer, Gerritsen, Houpt, & Levine, 1995) for quantitative pH determination in living cells with the fluorescent probe c.SNAFL-1. It was found that a lifetime-based approach was easier to employ than the traditional intensity-based ratiometric, while still providing accurate information regarding intracellular pH. Another FLIM-based pH measurement was presented in Lin, Herman, and Lakowicz (2003), which suggested that FLIM can be employed to measure the intracellular pH of resting cells, and to follow the pH fluctuations inside cells after environmental perturbations.

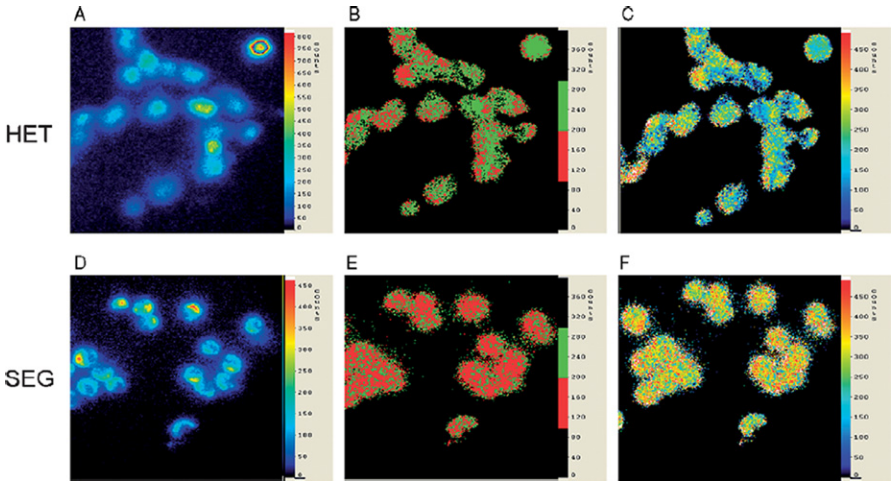

FIGURE 20.5

RTDP fluorescence intensity (A and D), lifetime in nanoseconds (B and E), and oxygen in micromolar (C and F) maps of normal human squamous esophageal epithelial cells (HET) (A–C) and Barrett's adenocarcinoma esophageal cells (SEG) (D–F). The intensity images (A and D) could not be reliably used to discriminate between the two different cell lines. The binary lifetime maps (B and E), on the other hand, plainly indicate different lifetimes for these two cellular species, with the SEG recording lower lifetimes than the HET. For the given case, $\tau_{HET} = 225$ ns and $\tau_{SEG} = 170$ ns. The mean lifetime difference was found to be $\Delta\tau = 44 \pm 7.48$ ns. Logically, this translated into higher oxygen levels in the SEG versus the HET using the calibration derived, as can be seen in the oxygen distribution maps (C and F) (Sud, Mehta, et al., 2006; Sud, Zhong, Beer, & Mycek, 2006).

Measurements of dissolved oxygen concentration in single living cells were previously demonstrated (Gerritsen, Sanders, Draaijer, & Levine, 1997; Mehta et al., 2007; Sud, Mehta, et al., 2006; Sud & Mycek, 2009; Sud, Zhong, Beer, & Mycek, 2006; Zhong, Urayama & Mycek, 2003), including one example shown in Fig. 20.5. Because the probe's fluorescence emission was found to be dynamically quenched by oxygen, the probe's lifetime was directly dependent upon local oxygen concentration and could be used for quantitative estimation of oxygen in living cells via FLIM. Molecular associations such as binding of the endogenous fluorophore nicotinamide adenine dinucleotide (NADH) to malate dehydrogenase have been imaged with FLIM (Lakowicz, Szmacinski, Nowaczyk, & Johnson, 1992) by using the increase in NADH lifetime upon binding as a source of contrast. NADH lifetime increased by ~150% and was much easier to detect than the blue shift of the emission spectrum that was only ~20% of the full-width at half-maximum in fluorescence intensity measurement.

Finally, FRET between the phospholipids NBD-PE (energy donor) and LRB-PE (energy acceptor) was employed to monitor endosomal fusion in single living cells

(Oida, Sako, & Kusumi, 1993). Excellent reviews providing further historical FLIM background can be found in French, So, Dong, Berland, and Gratton (1998), Gadella (1999), Tadrous (2000), van Munster and Gadella (2005), and Wallrabe and Periasamy (2005).

20.2 METHODS FOR CREATING FLUORESCENCE LIFETIME MAPS

The objective of both TD and FD measurements is to recover the lifetime parameter that describes fluorescence decay, thereby providing additional information that is not measured during steady-state intensity measurements. Both TD and FD methods (equivalent and related by the Fourier Transform) have comparable temporal resolution and discrimination, and benefit from the continual evolution of imaging technologies. The choice of FLIM instrumentation therefore depends on the particular application: FD FLIM uses any continuous wave light source and is better suited for evaluating short-lifetime measurements, while TD FLIM is optimal for flexible, large temporal range systems, and especially apt for long-lifetime measurements.

A more thorough and mathematically rigorous discussion of TD and FD approaches can be found in the previous edition of this book (Chang et al., 2007). In this edition, we emphasize emerging data analysis methods for FLIM (Section 2.3) that have been employed since the publication of the previous edition.

20.2.1 Time domain

Measuring fluorescence lifetime (τ) via TD methods involves reconstructing the exponential decay of fluorescence intensity over time, which can be accomplished in a variety of ways including the most commonly used techniques of gated integration and time-correlated single photon counting (TCSPC), each of which is further described below.

20.2.1.1 Time-gated FLIM

Figure 20.6 illustrates the instrumentation and concepts of the gated integration TD approach for measuring lifetime τ. A mode-locked or cavity-dumped laser, or a discharge source, is typically used to provide pulsed excitation. The excitation light pulse is split by a beam-splitter into two paths, one of which excites the sample on the microscope stage, while the other triggers the timing of an electronically gated charge-coupled device (CCD) camera, with programmable timing delays. After sample excitation, the fluorescence emission is collected by the CCD during gated detection. During the time period the CCD gate is open, the received fluorescence intensity signal is integrated (a convolution with the gated detector gain). Gates with different temporal delays provide different regions of the recorded signal waveform, making it possible to reconstruct the exponential decay curve.

Following the instrumentation setup in Fig. 20.6, the resulting fluorescence is a convolution of the sample's intrinsic fluorescence decay with the excitation

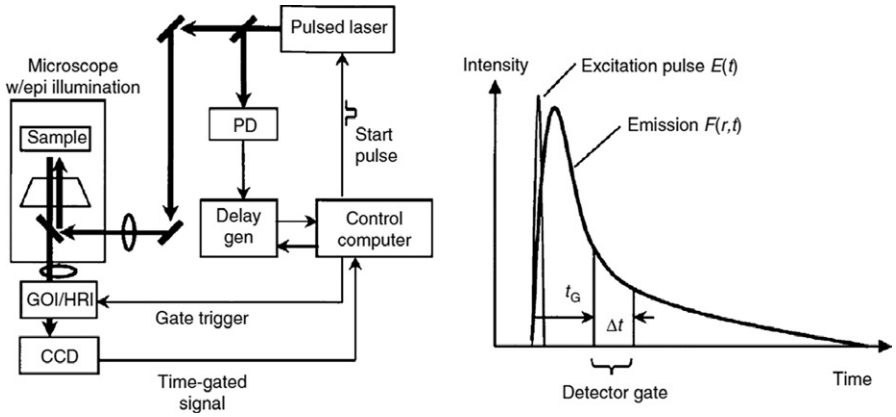

FIGURE 20.6

Time-domain lifetime imaging instrumentation and concepts (Sud, Mehta, et al., 2006; Sud, Zhong, Beer, & Mycek, 2006; Urayama & Mycek, 2003). The variable *r* indicates parameters that are spatially varying. Abbreviations for instrument schematics: PD, photodiode; delay gen, delay generator; GOI, gated optical intensifier; HRI, high-rate imager; CCD, charge-coupled device (camera); thick solid lines, light path; thin solid line, electronic path.

profile (the instrument response function) $E(t)$. For a sample with a spatially dependent j-component multiexponential lifetime, the fluorescence signal $F(r, t)$ is therefore

$$F(r,t) = E(t) \otimes \sum_j \alpha_j(r) \mathrm{e}^{-\left(\frac{t}{\tau_j(r)}\right)} = \int_{-\infty}^{t} E(t') \sum_j \alpha_j(r) \mathrm{e}^{-\left(\frac{t-t'}{\tau_j(r)}\right)} \mathrm{d}t' \tag{20.5}$$

where $\tau_j(r)$ and $\alpha_j(r)$ are the lifetime and amplitude of the jth component, respectively. The variable r emphasizes the spatial dependence of the fluorescence lifetime such as a pixel location on an area detector (e.g., a CCD camera). $E(t)$ is determined by replacing the sample with a reference with very short lifetime (unresolvable by system), so that the decay is effectively a delta-function. With $E(t)$ known, the lifetime $\tau_j(r)$ is fit to measured decays by using deconvolution algorithms, such as least-squares iterative reconvolution.

Because $F(r, t)$ detection must preserve both spatial and temporal information, a gated intensified CCD (ICCD) camera is often used. The ICCD can be switched on and off within a few nanoseconds, allowing it to control the exact timing of the signal incident onto the CCD. The fluorescence is imaged during a short interval $G(t)$

representing the gated detector gain, characterized by a rise time, fall time, and gate width. For a gate opening at time t_G, the detected image $D(r,t_G)$ is given by

$$D(r,t_G) = \int_{-\infty}^{\infty} G(t' - t_G)F(r,t')\mathrm{d}t' \tag{20.6}$$

The temporally and spatially resolved decay of the sample fluorescence is then reconstructed by imaging at various t_G, which is synchronized to the excitation pulse by using a photodiode coupled with electronics capable of variable delays.

However, deconvolution using iterative algorithms requires a well-sampled signal profile and can be computationally intensive and is usually not practical. Instead, pico- and femto-second sources, which can be regarded as delta-function excitation sources (time response is faster than system), are employed to eliminate the need for $E(t)$ deconvolution because fluorophore lifetimes are in the 0.1- to 10-ns regime. Also, the effects of $G(t)$ convolution can be minimized by using ratios of detected intensities (described in Section 2.3.1) or ICCD's with gate widths as fast as tens of picoseconds (Dowling, Hyde, Dainty, French, & Hares, 1997), so that $G(t)$ deconvolution may not be necessary.

20.2.1.2 TCSPC FLIM

In addition to gated detection, TCSPC has also been implemented for TD FLIM (Becker, Bergmann, & Weiss, 2002; Böhmer et al., 2001; Bugiel, König, & Wabnitz, 1989; Ghiggino, Harris, & Spizzirri, 1992). Figure 20.7 illustrates the concepts of TCSPC. The sample is excited with a high repetition rate excitation

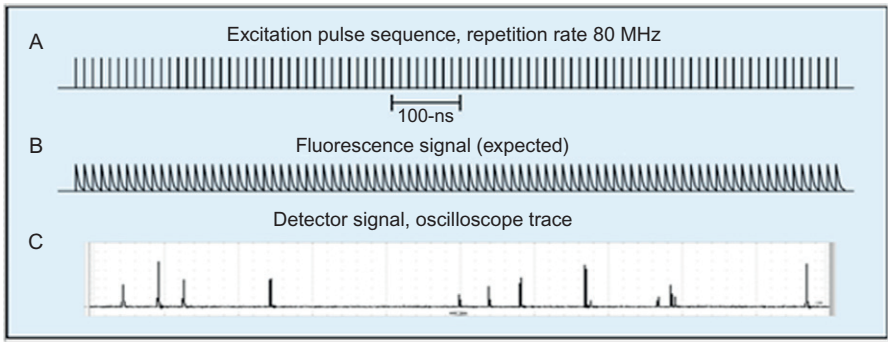

FIGURE 20.7

Illustration of time-correlated single photon counting (TCSPC). (A) A pulsed excitation source, here shown with a repetition rate of 80 MHz, is employed to repetitively excite a sample. (B) The expected fluorescence signal, if measured from each excitation pulse, would approximate an exponential pulse train. (C) However, the detected signal, here measured by an oscilloscope, is visibly different to that in part (B). The measured pulses are the detection of a single photon event, typically measured at a rate near $10^7\ \mathrm{s}^{-1}$. Once binned across time, these single observed fluorescence events accumulate into a fluorescence decay similar to Fig. 20.6 (right) (Becker, 2012).

source. With a sample with high quantum yield, each excitation pulse could generate a detectable fluorescence decay. In practice, this is not the case. Two primary reasons are users employing low excitation energy to limit potential photodamage to biological samples and weakly fluorescent samples. Therefore, TCSPC instead records fluorescence events with single-photon sensitivity and with time-correlated memory. Such memory records the first detected fluorescence photon as well as the time associated with the photon, and does not measure any later fluorescence. Therefore, the user can create a time-correlated histogram by binning individual recordings at the same time frames. TCSPC can be very accurate as the accuracy of the time measurement is not limited by the width of the detector gate. In addition, TCSPC has high efficiency, which records nearly every fluorescence photon detected, as compared with the time-gating scheme.

For TCSPC measurements (Lakowicz, 2006), a photomultiplier tube (PMT) is used to monitor each excitation pulse in order to produce a start signal to trigger the voltage ramp of a time-to-amplitude converter (TAC), which will be stopped upon detection of first emitted photon, providing an output pulse with a voltage proportional to the time between the start and stop signals. A multichannel analyzer converts the voltage to a time channel using an analog-to-digital converter (ADC). According to different time bins, where the photons are recorded, a probability histogram of counts is constructed versus time channels, from which the waveform of exponential decay is revealed.

An alternative is the reversed start–stop scheme, in which for each time period, the TAC is activated and starts ramping up voltage when the first photon is received. The voltage increase is stopped when a pulse is received, which can be either the pulse from the next period, or, if considering possible jitter of the pulses, a delayed pulse from the same period (the pulse that actually excited the photon). The reversal of time axis in the final data can be compensated for electronically. The advantage of the reversed start–stop scheme is that the TAC does not have to be constantly activated and reset in every period, considering the fact that in most periods actually no photon is recorded. However, reversed start–stop may cause some type of counting loss distortion.

With excitation pulses, dead-time-related distortion (one type of counting loss effect) may occur when using reversed start–stop scheme, since TAC/ADC dead time (when the TAC/ADC is processing signals) may extend into a subsequent pulse period. This will favor photon recording in the later part of pulse period. Dead-time-related distortion cannot be easily corrected, because the dead time may vary with the TAC voltage, and the transition from the dead time to the next active time may cause ripple in the TAC characteristic (Becker, 2005).

The photon counting rate is usually set to be only $\sim$1% to avoid a pile-up effect (another type of counting loss effect). The pile-up effect distorts the TCSPC data and makes the decay appear faster than is the case, since any photons detected after receiving the first photon will not be recorded. Simulations have been done to characterize the pile-up effect (Demas, 1983; Salthammer, 1992). The counting loss effect and its correction are described in Becker, 2005.

20.2.2 Frequency domain

The basic principle of FD FLIM is illustrated in Fig. 20.8 for a wide-field imaging system, though this approach is readily applicable to confocal systems (Fig. 20.9; Booth & Wilson, 2004). A sinusoidally modulated light source is used for excitation.

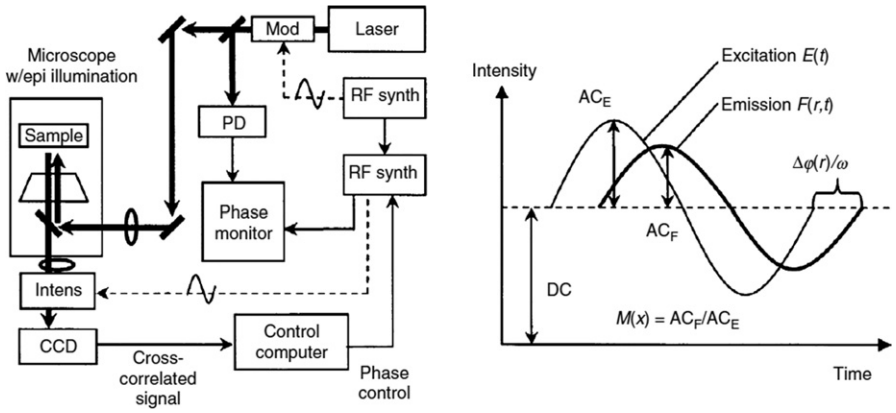

FIGURE 20.8

Frequency-domain lifetime imaging instrumentation and concepts (Urayama & Mycek, 2003). The variable *r* indicates parameters that are spatially varying. Abbreviations for instrument schematics: PD, photodiode; CCD, charge-coupled device (camera); RF synth, RF synthesizer; mod, intensity modulator; thick solid lines, light path; thin solid line, electronic path; dashed line, RF signal path.

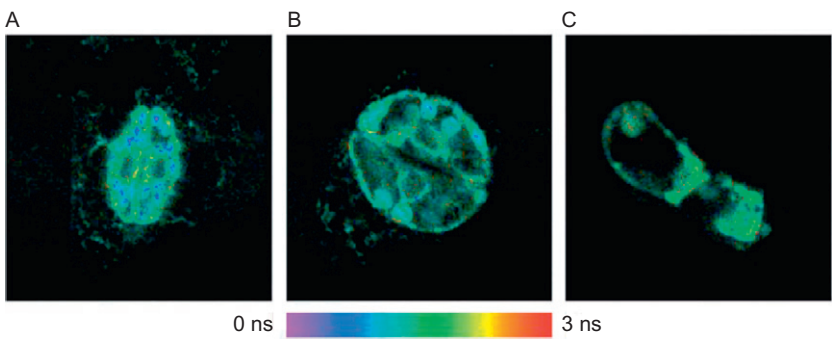

FIGURE 20.9

Combined fluorescence intensity and phase lifetime images of *Nicotiana tabacum* specimens with a confocal system. The fluorescence is a combination of autofluorescence and GFP fluorescence. (A and B) Stomata of leaves in which the endoplasmic reticulum was labeled with GFP5. (C) A trichrome of a leaf with GFP5-labeled Golgi. The hue of the images represents the fluorescence lifetime corresponding to the scale shown from 0 to 3 ns. The image widths are: (A) 100 μm, (B) 70 μm, and (C) 65 μm (Booth & Wilson, 2004).

The resulting sample emission is also sinusoidally modulated at the same frequency as the excitation, but is shifted in phase and is demodulated to some extent, that is, has a reduced modulation depth. Fluorescence lifetime can be directly calculated by changes in phase delay and demodulation. For measuring different lifetimes, different modulating source frequencies need to be used. Note that the measured phase delay φ between excitation and emission is in the range 0–90°, although arbitrarily long delays (>90°) can be introduced by optical delay lines. Demodulation of the emission is measured as a factor M (Fig. 20.8), which has a value of 0–1. It follows that at low frequencies, emission from samples with low lifetimes (fast decays) will follow the excitation faithfully; hence, the phase delay will be nearly 0° and the demodulation nearly 1. As the modulation frequency is increased, the finite lifetime of the fluorophore prevents this and is reflected in a phase delay as well as demodulation of the emission. At extremely high excitation frequencies, phase delay will be 90° while demodulation will be 0.

The phase delay and demodulation, plotted over a range of frequencies, provide the frequency response of the sample. Typically, the plot is limited to a "useful frequency" range in which changes in phase and demodulation are frequency dependent. As a general rule, the center frequency of this plot is approximately the reciprocal of the fluorescence lifetime (i.e., $1/\tau$). Hence, typical biological fluorophores such as NAD(P)H and collagen with lifetimes of few nanoseconds need excitation sources modulated at 1–200 MHz. Long-lived fluorophores such as platinum and ruthenium–ligand complexes have lifetimes of microseconds and hence the modulation is tens of kHz to 1 MHz. Lifetimes in the low picoseconds (e.g., Rose Bengal, 90 ps) require modulated sources at frequencies of approximately 2 GHz.

A detailed treatment of standard FD FLIM instrumentation and its variants can be found elsewhere (Lakowicz, 2006). Briefly, radio frequency modulation (MHz range) of a light source is done via acousto- or electro-optic modulators. The light source can be CW (argon-ion laser, arc lamps) or even a high repetition rate pulsed laser. On the detection side, cross-correlation is used to extract low-frequency phase and demodulation information by modulating the detector at a frequency offset from the modulation frequency, a scheme known as heterodyne detection. For sync operation, the same RF synthesizer is hence used for modulating the light source as well as providing the reference signal for the intensifier on the CCD.

One difficulty of FD measurements is accurate estimation of phase angle and modulation at high frequencies. In heterodyne detection, the signal waveform at the modulation frequency F is convolved with a reference waveform at frequency $F + \Delta F$ ($\Delta F = 10$–100 Hz). The slow response of the CCD acts as a low-pass filter that removes the high frequency component in the resulting waveform and provides an easily detectable, slowly varying signal with the phase and modulation information. Another approach known as homodyne detection involves setting $\Delta F = 0$. The resulting signal (after low-pass filtering) is a static-phase-dependent signal. A detailed treatment of FD data analysis can be found in Urayama and Mycek (2003).

20.2.3 Data analysis methods

FLIM measures a three-dimensional data cube, containing both spatial and temporal information. Analyzing FLIM measurements is, therefore, more involved than analyzing intensity-based measurements. Five methods are introduced in this section: (i) rapid lifetime determination (RLD) and analytical least-squares algorithms, (ii) iterative least-squares analysis with multiexponential fitting, (iii) least-squares analysis with Laguerre polynomial fitting, (iv) phasor plot analysis, and (v) methods for improving precision of fluorescence lifetime maps. Methods detailed focus on rapid, accurate, and high-throughput FLIM analysis.

20.2.3.1 RLD and analytical least-squares algorithms

An analytic RLD algorithm can be used to analyze time-gated FLIM data (Bugiel et al., 1989; Sharman, Periasamy, Ashworth, Demas, & Snow, 1999; Wang, Uchida, Coleman, & Minami, 1991). As an example of how using intensity ratios eliminate gate parameters and of analytic lifetime determination, consider a sample with a single-exponential lifetime excited by a negligibly short excitation pulse. For an effective gate width Δt, the gated detector signal at time t is as follows

$$D(r,t) = \int_{t}^{t+\Delta t} \alpha e^{-\left(\frac{t'}{\tau(r)}\right)} dt' = \alpha\tau\left[e^{-\left(\frac{t}{\tau(r)}\right)} - e^{-\left(\frac{t+\Delta t}{\tau(r)}\right)}\right] \tag{20.7}$$

A spatially resolved lifetime τ (r) can be determined by using two images gated at times t_1 and t_2 (Wang, Periasamy, Herman, & Coleman, 1992), so that

$$\tau(r) = \frac{t_2 - t_1}{\ln\frac{D(r,t_1)}{D(r,t_2)}} \tag{20.8}$$

Note that the gate width cancels from the ratio. Because the lifetime determination is analytic and requires only two gates, a two-dimensional image of lifetimes can be constructed rapidly. The acquisition of only two gates allows one to measure the lifetime map in real time, since image acquisition and processing take a fraction of a second (Cubeddu, Comelli, D'Andrea, Taroni, & Valentini, 2002). In practice, a two-gate scheme can be sensitive to noise, therefore methods using N gates (N typically equal to 5–10; Cubeddu et al., 2002) can be used with least-squares method to increase data redundancy and give more stable results. In this case, lifetime images were calculated on a pixel-by-pixel basis by

$$\tau_p = -\frac{N\left(\sum t_i^2\right) - \left(\sum t_i\right)^2}{N\sum t_i \ln I_{i,p} - \left(\sum t_i\right)\left(\sum \ln I_{i,p}\right)} \tag{20.9}$$

where N is the number of images, $I_{i,p}$ is the intensity of pixel p in image i, and t_i is the gate delay of image i. All sums are over i.

For more complicated fluorescence decays, double exponential (Cubeddu et al., 2002; Sharman et al., 1999) and nonexponential decays (Lee et al., 2001) have been considered.

20.2.3.2 Iterative least-squares analysis with multiexponential fitting

Iterative least-squares analysis can be performed to analyze TCSPC-FLIM data. The goal of iterative least-squares method is to minimize goodness of fit (χ^2) by varying the values of model parameters. χ^2 is expressed as follows

$$\chi^2 = \sum_{k=1}^{n} \frac{1}{\sigma_k^2} [N(t_k) - N_c(t_k)]^2 = \sum_{k=1}^{n} \frac{[N(t_k) - N_c(t_k)]^2}{N(t_k)} \tag{20.10}$$

where n is the total number of channels, $N(t_k)$ is the observed count number in channel k, $N_c(t_k)$ is the calculated count number in channel k from model prediction, and σ_k^2 is the variance of $N(t_k)$, which is equal to $N(t_k)$ from Poisson statistics. χ^2 is actually a variance-weighted least-squares statistic that will have a value close to the number of measurements channels for good fits, which follows statistical χ^2 distribution.

Suppose the FLIM data are being analyzed in terms of the multiexponential model in Eq. (20.5), then the values of τ_j and α_j are varied until χ^2 is a minimum, which occurs when $N(t_k)$ and $N_c(t_k)$ are most closely matched. In practice, a table of χ_R^2, reduced χ^2 (defined as the division of χ^2 by the degrees of freedom) distribution, showing the p-values for various χ_R^2 values with different degrees of freedom, will help decide how well the model fits the data. Since systematic errors in the data can easily result in a 10–20% elevation of χ_R^2, a model would be acceptable if p-value is not statistically significant at 5% significant level (Lakowicz, 2006).

20.2.3.3 Least-squares analysis with Laguerre polynomial fitting

The Laguerre deconvolution method was proposed for time-resolved fluorescence analysis in 1993 (Marmarelis, 1993), first being demonstrated for rapid analysis of single fluorescence decays and only recently demonstrated for fast FLIM analysis (Jo, Fang, & Marcu, 2005; Pande & Jo, 2011). Since then, Laguerre analysis has been employed for a variety of fluorescence lifetime and FLIM applications, ranging from brain tumor (Sun et al., 2010) to oral carcinoma detection (Sun et al., 2009). Advantages of Laguerre deconvolution compared with multiexponential fitting include no *a priori* assumptions about the modeled decay behavior of the data, rapid fitting via least-squares estimation, and a unique "best" fit.

Laguerre analysis is based on the Laguerre expansion of the kernel technique. Each measured decay is fit to one set of unique and discrete Laguerre functions on an orthonormal basis given as follows

$$h(r,n) = \sum_{j=0}^{L-1} c_j(r) b_j^{\alpha}(n) \tag{20.11}$$

with

$$b_j^{\alpha}(n) = \alpha^{(n-j)/2}(1-\alpha)^{1/2}\sum_{k=0}^{j}(-1)^k\binom{n}{k}\binom{j}{k} \tag{20.12}$$

where $c_j(r)$ are the Laguerre expansion coefficients to be solved for at each pixel p, L is the number of Laguerre functions to be used to model the fluorescent data, and $b_j^{\alpha}(n)$ represents the jth Laguerre function. The α value used must be between 0 and 1. For fluorescence decays with longer average lifetimes, higher α values will yield better fits.

Laguerre analysis has been employed for FLIM analysis because the model can fit each image pixel simultaneously. Such an approach has been shown to reduce analysis time by at least two orders of magnitude (Jo et al., 2005). For example, in 480×736 FLIM images, Laguerre analysis was shown to take <60 s (Sun et al., 2010).

20.2.3.4 Phasor plot analysis

Phasor plot analysis is based on well-established procedures originally developed to analyze dielectric relaxation experiments, that is, a sample's transient responses to repeated perturbations (Hill, 1969). In fluorescence, this method was applied to analyze FD FLIM data, as the modulated excitation light is the perturbation and the fluorescence emission is the relaxation. In recent years, phasor analysis was further developed to offer a simple, graphical, and rapid algorithm for interpreting FD FLIM data that were obtained after single excitation frequency from samples exhibiting more than one fluorescence lifetime (Clayton, Hanley, & Verveer, 2004; Redford & Clegg, 2005).

In FD experiments, phasor analysis transformed the modulation, M, and the phase, φ, (see Fig. 20.8) of the emission with respect to the excitation into

$$x = M\cos\varphi \tag{20.13}$$

and

$$y = M\sin\varphi. \tag{20.14}$$

A pair of x and y values represents a phasor vector on the phasor plot.

TD FLIM can also be analyzed with phasor analysis because the excitation pulse frequency can be transformed into phasor space similarly to the sinusoidal excitation frequency of FD FLIM. To provide an instantaneous (excluding complex fitting procedures) view of the fluorescence decay in TD experiments, the FD FLIM phasor plot analysis was modified (Digman, Caiolfa, Zamai, & Gratton, 2008). Fluorescence decays, $F(t)$, at each pixel of an image were transformed into a phasor plot by

$$x = \frac{\int_0^{\infty} F(t)\cos(\omega t)\mathrm{d}t}{\int_0^{\infty} F(t)\mathrm{d}t} \tag{20.15}$$

and

$$y = \frac{\int_0^\infty F(t)\sin(\omega t)\mathrm{d}t}{\int_0^\infty F(t)\mathrm{d}t}, \tag{20.16}$$

where ω is the laser repetition angular frequency. Each pixel of the image gives a point on the phasor plot. If the fluorescence decay is single exponential, the coordinates x and y become

$$x = \frac{1}{1+(\omega\tau)^2} \tag{20.17}$$

and

$$y = \frac{\omega\tau}{1+(\omega\tau)^2}. \tag{20.18}$$

The two coordinates lie on the semicircle of a phasor plot, as shown in blue in Fig. 20.10A.

The analysis is performed by observing clustering of pixels in specific regions of the phasor plot, providing a global view of FLIM images. The method can also be used in a reciprocal mode in which each point of the phasor plot is mapped, and pseudocolored, to a pixel of the image (Fig. 20.10). Since every molecular species has a specific phasor vector, located in specific regions, users can identify molecules by their position on the phasor plot. Therefore, the phasor/polar plots analysis makes the interpretation of FLIM data accessible to the nonexpert.

20.2.3.5 Improving precision of fluorescence lifetime maps

Precise fluorophore lifetime mapping is vitally important to quantifying the biological microenvironment. One challenge to precise lifetime mapping is that all measurements must be obtained without perturbing living cells—a difficult task. The experimenter may be tempted to use high power and long measurement times to acquire high-quality images, but such conditions could damage the cells and fluorophores. The opposite can also be true. Low-light and fast measurements will maintain cell viability, but may not produce images with high signal-to-noise ratio. Temporal optimization and spatial denoising methods were developed to address this problem and enhance the precision of acquired FLIM data.

For time-gated FLIM, optimal temporal gating techniques using either Monte Carlo simulations or analytical error propagation analysis were developed to reduce the illumination light dose, while additionally improving the precision of lifetime analysis (Chang & Mycek, 2010b; Sharman et al., 1999). Relative standard deviation (RSD), defined as the standard deviation divided by the mean value, was calculated over a determined FLIM image assuming only Poisson noise. The optimal gating parameters, the gate width and the time interval between the starting points of

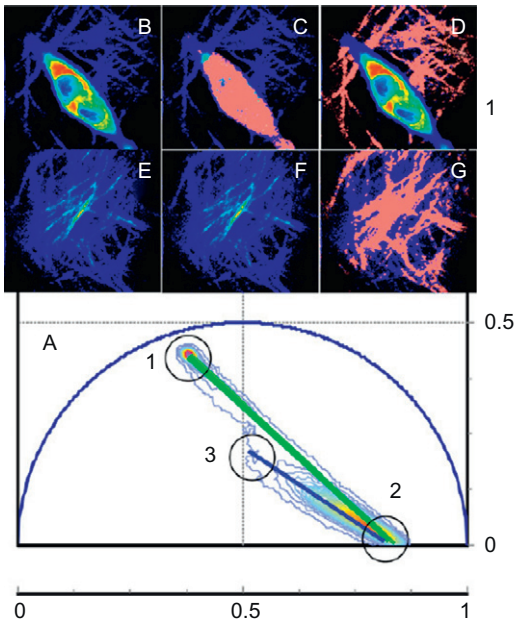

FIGURE 20.10

Phasor plot analysis for analyzing time-domain FLIM data offers several key advantages compared with conventional time-domain FLIM data analysis techniques. The analysis is instantaneous without complex fitting procedures and the phasor plot provides a visual representation of the fluorescence decay, making the FLIM technique accessible to an untrained user. Here, fluorescence intensity images were acquired from (B) CHO-K1 cells transfected with paxillin EGFP in a three-dimensional collagen matrix and (E) only the collagen matrix. Each fluorescence image pixel was transformed into (A) phasor space. All pixels contained within cursor Position 1 on the phasor plot were pseudocolored pink in images (C) and (F), corresponding to the EGFP expression. The pixels contained within Position 2 were pseudocolored pink in images (D) and (G), corresponding to the collagen fluorescence. Position 3 represents weak fluorescence background. The color-coded images show homogeneous EGFP or collagen signals, demonstrating a precise characterization of the cellular microenvironment (Digman et al., 2008).

two consecutive gates, were determined by minimizing the RSD. In addition to optimal temporal gating, image denoising methods were employed to enhance time-gated and TCSPC-FLIM data for precise lifetime mapping.

Figure 20.11 shows that both optimal virtual gating and the total variation (TV) denoising method, commonly used in medical imaging systems for selective smoothing and hence edge preserving, reduced RSD of TCSPC-FLIM data in live cells (Chang & Mycek, 2010a). In particular, when combining the two methods sequentially, the resulting RSD was lower than when either method was employed alone. One advantage of this newly developed, TV-based spatial denoising method

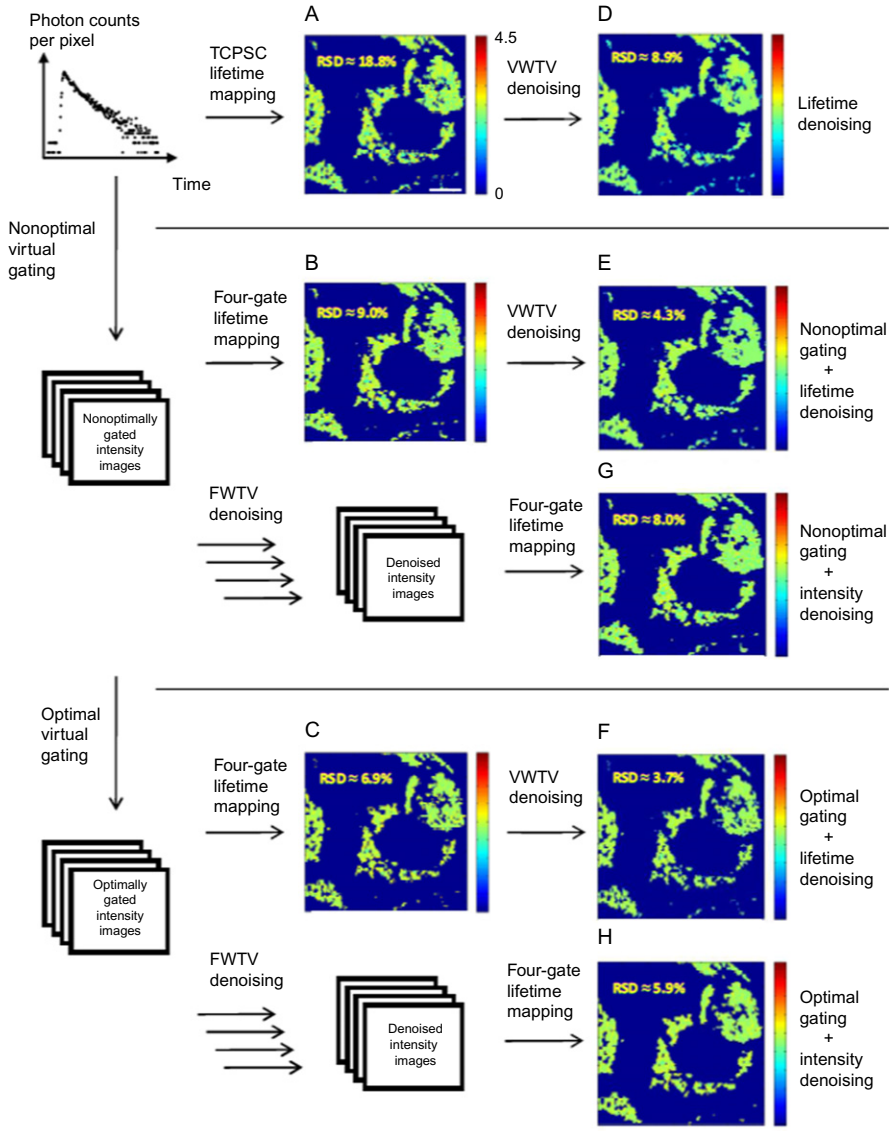

FIGURE 20.11

Temporal optimization and spatial denoising methods can be applied to previously acquired FLIM measurements to improve lifetime precision of live-cell images. Here, multiphoton microscopy was employed to image live LLC-PK1 cells expressing mEmerald-EB3. Temporal optimization improved lifetime precision shown from (A) the TCSPC lifetime map to (C) the optimal virtual-gated lifetime map, indicated by the decreased RSDs. Total variation denoising techniques further improved lifetime precision, yielding reduced RSDs in (D)–(H). In addition, employing the denoising method combined with optimal virtual gating notably improved the precision of (C). RSD represents relative standard deviation, an indicator for the lifetime uncertainty. FWTV, *f*-weighted total variation; VWTV, variance-weighted total variation (Chang et al., 2010a).

is its versatility: the technique can be employed to denoise intensity images at each gate or it can directly denoise a lifetime map with either Poisson or non-Poisson distributed noise (Chang & Mycek, 2010a, 2010b, 2012a).

20.3 FLIM TECHNIQUES FOR QUANTITATIVE BIOLOGICAL IMAGING

The applications that follow are examples of FLIM that were chosen to highlight the broad range of FLIM applications, spanning both endogenous and exogenous fluorescence measurements. These measurements include subcellular resolution to detect protein–protein interactions (e.g., FRET) and molecular diffusion (e.g., FCS). Additionally, the examples demonstrate applications of FLIM for quantitative biological imaging via exogenous and/or sample endogenous fluorophores for several biological systems, including cells, tissues, and organs.

20.3.1 FLIM detection of FRET events

Förster (or fluorescence) resonance energy transfer theory was developed by Professor Theodor Förster (Förster, 1948), and it describes the mechanism for experimental techniques developed to measure spatial distance between two (or multiple) fluorophores. Cell biologists exploit FRET to measure the distance between two sites on a macromolecule, the distance between two proteins attached with fluorophores, and hence whether and how these two proteins interact. FRET is regarded as an *in vivo* "nanoscale ruler," since it can be monitored in living cells, and the distance for FRET to occur is usually within several nanometers, and on the same scale as the dimensions of biological macromolecules. The diameter of many proteins, the distance within which proteins interact in living cells, the thickness of biological membranes, and the distance between sites on multisubunit proteins are typically within this scale.

FRET mandates the presence of at least one donor–acceptor (D–A) pair having a D–A distance associated therewith, although more than one such pairs and hence distances can be involved. Readers interested in more details are referred to Chapter 15 in Lakowicz, 2006. FRET occurs when the donor emission spectrum overlaps with the acceptor excitation spectrum. After donor excitation, energy will be transferred nonradiatively if the D–A pair is in close proximity (i.e., via the nonradiative pathway illustrated in Fig. 20.2 without photo emission), as a result of long-range dipole–dipole interaction between the D–A pair. In other words, the acceptor does not reabsorb the photons emitted from the donor as a means of energy transfer, which also implies that the intervening solvent or molecule has little effect on the efficiency of FRET. A common use of FRET is to monitor any phenomena with changes in the D–A distance, such as conformational changes of a macromolecule, or the cleavage of a macromolecule by enzymes. FRET can be measured with endogenous (using tryptophan as a donor, Table 20.1) or exogenous fluorophores (e.g., CFP-YFP) as D–A pairs in cell biology (Becker et al., 2005).

How close exactly for the D–A pair will FRET occur? Quantitatively, Förster distance is defined as the distance at which the energy transfer efficiency is 50% and the energy transfer efficiency (E) is defined as

$$E = \frac{k_T}{\tau_D^{-1} + k_T} \tag{20.19}$$

where τ_D is the donor lifetime in the absence of an acceptor and k_T is the energy transfer rate from a donor to an acceptor. k_T is given by

$$k_T = \frac{1}{\tau_D}\left(\frac{R_0}{r}\right)^6 \tag{20.20}$$

where R_0 is the Förster distance and r is the D–A distance. In Eq. (20.20), when $r = R_0$, $E = 50\%$, as described in the definition of Förster distance. Also, the dependence of k_T on r is highly nonlinear and strong when the D–A distance is near R_0; when $r = 2R_0$, the energy transfer efficiency drops to only 1.56%, according to Eqs. (20.19) and (20.20).

In order to detect FRET efficiently, D–A pairs with longer R_0 are preferred. The typical value of R_0 is in the range of 20–60 Å, depending on the extent of D–A spectra overlap, the D–A orientation, the refractive index of the medium, and the quantum yield (see Eq. 20.4) of the donor in the absence of an acceptor. Since D–A orientation is usually assumed to be dynamic and random, while refractive index of the medium typically treated as a constant for biomolecules in aqueous solution, in usual cases R_0 is considered dependent only on the optical properties of the fluorophore pairs and is approximately fixed for a given D–A pair.

FRET can be measured with either steady-state or time-resolved data (Jares-Erijman & Jovin, 2003); the donor lifetime is shortened and the donor intensity is lowered if FRET occurs. FRET-FLIM combines FRET and lifetime imaging, often with considerable advantages over intensity-based FRET. The main advantage is that FRET-FLIM eliminates possibilities that results are biased from intensity-based measurement artifacts that could modify results by more than the FRET efficiency (Chang, Wu, Merajver, & Mycek, 2009; Zhong et al., 2007).

Figure 20.12 presents results from a time-lapsed FRET-FLIM study that measured chromatin compaction at the scale of nucleosomal arrays in live cells from metaphase to telophase (Lleres et al., 2009). A human cell line coexpressing histone H2B tagged to express either enhanced green fluorescent proteins (EGFP) or mCherry fluorescent proteins was monitored. FRET occurred between EGFP- and mCherry-tagged histones on separate nucleosomes. The number of FRET events increases when chromatin compacts. The FRET map spatially illustrated the degree of compaction for the entire set of chromosomes (Fig. 20.12). A heterogeneous population of different FRET efficiencies was seen in metaphase (blue and green regions), which subsequently became more homogeneous and reached maximum as the cell progressed into late anaphase. These data are consistent with extensive higher order folding of chromatin fibers occurring during the anaphase.

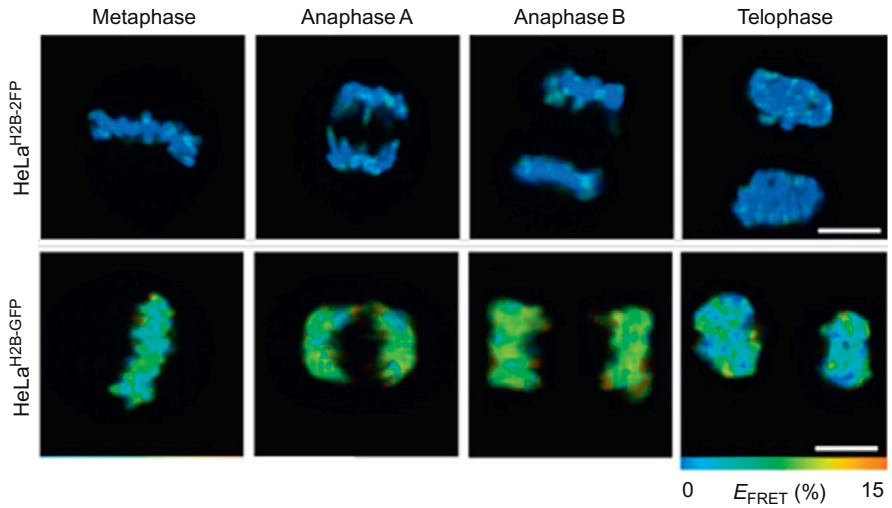

FIGURE 20.12

FLIM-FRET was used to assess chromatin compaction within chromosomes of live cells at different stages of mitosis. FRET map derivation is detailed in Section 3.1. HeLa cells (top, control) expressing only histone H2B tagged to enhanced green fluorescent protein (EGFP) ($HeLa^{H2B\text{-}GFP}$) or (bottom, experimental) coexpressing H2B tagged to either EGFP or mCherry FPs ($HeLa^{H2B\text{-}2FP}$) were compared. FRET occurs between FP-tagged histones and was increased during chromatin compaction. $HeLa^{H2B\text{-}2FP}$ cells at different stages during mitosis show variations in compaction level, observed as different FRET efficiency populations. The variation was throughout the length of all chromosomes, reaching maximum FRET efficiency in late anaphase. Alternatively, $HeLa^{H2B\text{-}GFP}$ did not show the FRET variation. Scale bar: 10 μm (Lleres, James, Swift, Norman, & Lamond, 2009).

In addition, a two-photon FRET-FLIM system for protein localization was characterized (Chen & Periasamy, 2004), and plasma membrane organization in cowpea protoplasts was studied using FRET-FLIM with different GFP-fused proteins (Vermeer, van Munster, Vischer, & Gadella, 2004). A FRET-FLIM-based detection, performed in FD, was employed to monitor protein kinase Cα (PKCα) molecules immunostained with both Cy3 (donor) and Cy5 (acceptor). FRET occurred only on phosphorylated PKCα molecules (Ng et al., 1999). A review on FRET-FLIM has provided a table of commonly used FRET fluorophore pairs for FLIM studies (Wallrabe & Periasamy, 2005).

20.3.2 Intracellular molecular diffusion rates measured via FCS-FLIM

The advent of photon counting techniques such as TCSPC has resulted in the development of statistical methods for sample analysis, broadly classified as FCS. As mentioned earlier, benefits of FLIM lie in obtaining information other than,

and complementary to, fluorophore concentration and localization; this includes the molecular environment and protein grouping and/or interactions. By measuring variations in fluorescence intensity at a single image pixel over time, FCS provides single-point measurements of kinetic and diffusion properties of fluorescent molecules, as well as their concentration and aggregation state. The detection volume in confocal systems is in the subfemtometer range, and the number of fluorescent molecules in this small space will typically be one.

FCS can also be used to cover dynamic phenomena on a submicrosecond timescale. FCS-FLIM provides a very useful fluorescence modality which can be implemented on confocal systems, and commercial integrated products are available for this purpose. FCS has been reported early on for studying the mobility of small solutes in the cytoplasm of living cells (Berland, So, & Gratton, 1995). Kask, Palo, Ullmann, and Gall (1999) used FCS for monitoring restriction-enzyme-mediated cleavage of DNA hybrids by using fluorescently labeled complementary oligonucleotides. A two channel confocal fluorescence lifetime microscope was used for FCS and FLIM, since the timing information down to a picosecond scale offered the possibility not only to reconstruct fluorescence decay of each pixel for FLIM but also to analyze the fluorescence fluctuation correlation function of any single spot of interest (Wahl, Koberling, Patting, Rahn, & Erdmann, 2004). Healthy and sorbitol-stressed cells expressing a GFP-MK2 fusion protein were studied with TCSPC and analyzed with lifetime imaging and FCS (Becker et al., 2006). In stressed cells, while FLIM results demonstrated a lifetime reduction and translocation of the proteins to the cytoplasm, FCS of one single spot showed slower diffusion with higher correlation amplitude, possibly indicating the aggregation of the proteins. Reviews on FCS and FLIM can also be found in Breusegem, Levi, and Barry (2006) and Hink, Bisselin, and Visser (2002).

20.3.3 Multispectral-FLIM

Multispectral-FLIM (ms-FLIM) leverages the primary advantages of fluorescence spectroscopy and FLIM imaging into one measurement (Becker, Bergmann, & Biskup, 2007; Lloyd et al., 2010). That is, ms-FLIM enables the user to perform spectral unmixing to isolate individual fluorophore contributions from a multi-fluorophore samples, akin to fluorescence spectroscopy, while additionally allowing the user to measure the effect of the microenvironment on an individual fluorophore in a given spectral band, akin to fluorescence lifetime imaging. Collecting FLIM images in multiple wavelength bands increases the overall measurement time, but the advantageous gains in data breadth described below can overcome such a limitation.

The advantages from fluorescence spectroscopy and FLIM imaging provide the most benefit when measured samples contain multiple fluorophores with broad emission spectra, whether exogenous, endogenous, or both. Such samples often contain a fluorophore that will be prominent in the collected signal, making the contributions from less prominent fluorophores very small and more difficult to analyze.

One advantage to FLIM imaging, as mentioned earlier, is the measurement of functional and spatial fluorophore information. ms-FLIM takes this one step further: through FLIM image acquisition at multiple wavelengths, functional information can be analyzed from multiple fluorophores. One such example involving endogenous fluorescence is the simultaneous detection of NAD(P)H and FAD, two biologically relevant molecules related to cellular metabolism. In this case, these fluorophores can be preferentially detected with emission detection less than ~500 nm for NAD(P)H and greater than ~500 nm for FAD (Skala et al., 2007).

Figure 20.13 shows typical data collected with an ms-FLIM instrument (Becker et al., 2007). Here, a fresh mouse kidney section was excited with 750-nm two-photon excitation, and images were collected in 16 evenly spaced wavelength

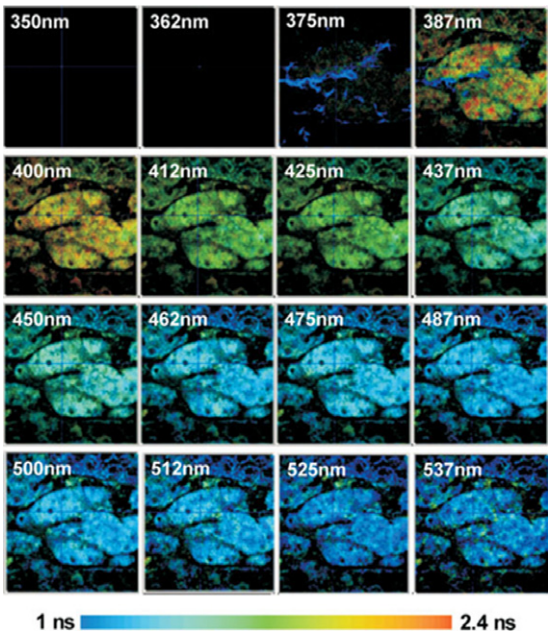

FIGURE 20.13

Multispectral fluorescence lifetime imaging microscopy (ms-FLIM) increases data depth of standard FLIM measurements. Here, ms-FLIM measurements were acquired by measuring FLIM images with a fixed excitation wavelength and varying emission wavelength bandpasses. Such data enable the user to spatially and spectrally resolve fluorescence. Here, ms-FLIM images were measured from unstained mouse kidney after 2-photon excitation at 750 nm (Zeiss LSM510 NLO microscope with Becker–Hickl FLIM detection). While characteristic fluorescence was similar among all wavelengths spatially, there are marked differences in average fluorescence lifetime, ranging from ~2–2.4 ns at 387 nm to ~1 ns or less at 537 nm, underscoring the ability for quantitative analysis of multiple tissue fluorophores (Becker et al., 2007).

regions from 350 to 537 nm. FLIM maps of average lifetime are shown for each wavelength region. There is an observable decrease in average lifetime from low-emission wavelengths (<400 nm) to middle-emission wavelengths (412–450 nm) to high wavelengths (>462 nm), which can be attributed to the detection of different relative contributions of endogenous fluorophores in each wavelength region. Collection time for the image was 10 min, resulting from a low power level to reduce sample photobleaching and photodamage. With a higher sample fluorescence, common in some applications involving exogenous fluorescence, multispectral images were collected in 20 s with a fixed excitation wavelength (Becker et al., 2007).

One future application of ms-FLIM can be for enhanced FLIM-FRET detection. With measurements in multiple wavelength ranges, the user will have an easier task to separate the donor and acceptor lifetimes. Additionally, it will be easier to separate out background fluorescence (Becker et al., 2007).

For greater fluorophore separation, state-of-the-art excitation sources can be combined with ms-FLIM setups to achieve multiwavelength detection after multiwavelength excitation (Owen et al., 2007). This application involves more selective fluorophore targeting than common ms-FLIM setups. Moreover, multiwavelength excitation allows for greater precision in resolving individual fluorophores and the effect of the microenvironment (Skala et al., 2007).

20.3.4 MP-FLIM of endogenous tissue fluorophores

Multiphoton excitation microscopy provides high axial (optical sectioning) and lateral resolution, reduced out of focus photobleaching/photodamage, and is optimal for deep tissue imaging (Helmchen & Denk, 2005). The high sensitivity of multiphoton microscopy imaging makes it ideal for measuring endogenous tissue fluorophores.

Endogenous tissue fluorophores such as NAD(P)H, FAD, collagen, elastin, and keratin report on tissue microenvironment without chemical staining (Zipfel et al., 2003). In particular, intracellular NAD(P)H and FAD molecules are involved in mitochondrial metabolic pathways (Heikal, 2010). Therefore, measurements of such endogenous fluorophores are label-free indicators of tissue metabolism.

Figure 20.14 illustrates NAD(P)H- and FAD-binding states measured with a multiphoton-FLIM system. *In vivo* label-free measurements to monitor precancerous epithelia were performed on 22 hamster cheek pouches (Skala et al., 2007). A significant decrease in the contribution and lifetime of protein-bound NADH was observed in both low- and high-grade epithelial precancers compared with normal epithelial tissues. In addition, a significant increase in the protein-bound FAD lifetime and a decrease in the contribution of protein-bound FAD were observed in high-grade precancers only. Increased intracellular variability in the NADH and FAD fluorescence lifetimes were observed in precancerous cells compared with normal cells.

Label-free multiphoton-FLIM was also employed to characterize normal human epidermis at different skin sites and in patients of different ages (Benati et al., 2011), monitor metastasis and the tumor microenvironment in tissues (Provenzano, Eliceiri, & Keely, 2009), and monitor cell viability for tissue engineering applications

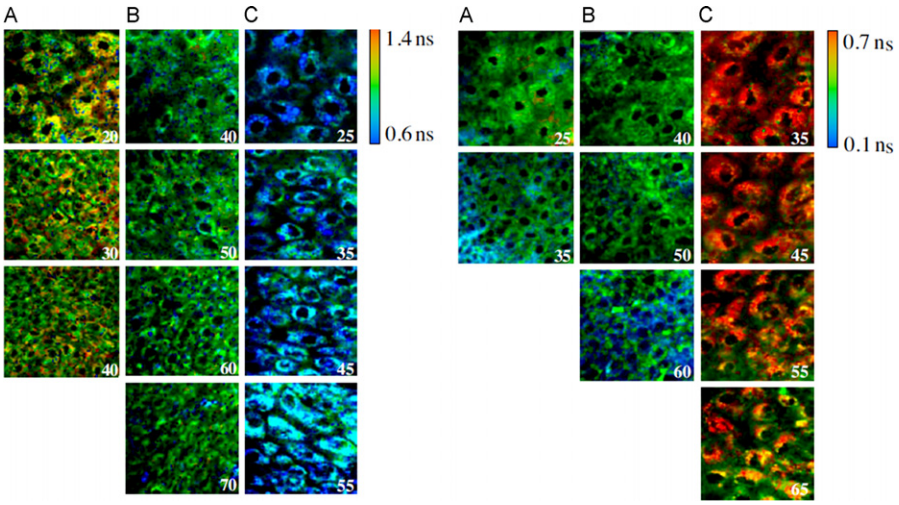

FIGURE 20.14

Multiphoton TCSPC-FLIM was employed to distinguish (A) normal, (B) low-grade precancer, and (C) high-grade precancer promoted in a hamster cheek pouch model. *In vivo* multiphoton TCSPC-FLIM images of (left) mean NADH and (right) mean FAD suggested that the averaged NADH lifetime decreases and the average FAD lifetime increases with precancer development. The lifetime and contribution of free and protein-bound NADH and FAD were shown to characterize the precancer development in Skala et al. (2007). Images were acquired with excitation at 800 nm and emission centering at 490 nm (with a 490 short-pass filter) for NADH, excitation at 890 nm and emission between 400 and 600 nm for FAD.

(Lloyd et al., 2012) via measurements of endogenous tissue fluorophores, demonstrating its potential for future clinical use.

SUMMARY

In this chapter, the basic concepts, key advantages, data analysis methods, and several applications of FLIM are discussed. Continuing advances in technology for microscopy and the developing appreciation that fluorescence lifetime is a sensitive means for quantitatively evaluating microenvironment will likely help make FLIM a critical research tool for cell biology by providing new ways for life scientists to detect, visualize, and investigate structure and function in biological systems.

Acknowledgment

This work was supported in part by the National Institutes of Health grant NIH R01-DE-01943 (to M.-A. M.).

References

Becker, W. (2005). *Advanced time-correlated single photon counting techniques* Vol. 81. Berlin, Heidelberg: Springer Verlag.

Becker, W. (2012). *The bh TCSPC handbook* (5th ed.). Berlin, Germany: Becker & Hickl GmbH. *http://www.becker-hickl.com/handbook.htm*.

Becker, W., Bergmann, A., & Biskup, C. (2007). Multispectral fluorescence lifetime imaging by TCSPC. *Microscopy Research and Technique*, *70*(5), 403–409.

Becker, W., Bergmann, A., Haustein, E., Petrasek, Z., Schwille, P., Biskup, C., et al. (2005). Fluorescence lifetime images and correlation spectra obtained by multi-dimensional TCSPC. *Multiphoton Microscopy in the Biomedical Sciences V*, *5700*, 144–151.

Becker, W., Bergmann, A., Haustein, E., Petrasek, Z., Schwille, P., Biskup, C., et al. (2006). Fluorescence lifetime images and correlation spectra obtained by multidimensional time-correlated single photon counting. *Microscopy Research and Technique*, *69*(3), 186–195.

Becker, W., Bergmann, A., & Weiss, G. (2002). Lifetime imaging with the Zeiss LSM-510. *Proceedings of SPIE*, *4620*, 30–35.

Benati, E., Bellini, V., Borsari, S., Dunsby, C., Ferrari, C., French, P., et al. (2011). Quantitative evaluation of healthy epidermis by means of multiphoton microscopy and fluorescence lifetime imaging microscopy. *Skin Research and Technology*.

Berland, K. M., So, P. T. C., & Gratton, E. (1995). Two-photon fluorescence correlation spectroscopy—Method and application to the intracellular environment. *Biophysical Journal*, *68*(2), 694–701.

Böhmer, M., Pampaloni, F., Wahl, M., Rahn, H.-J., Erdmann, R., & Enderlein, J. (2001). Time-resolved confocal scanning device for ultrasensitive fluorescence detection. *The Review of Scientific Instruments*, *72*(11), 4145–4152.

Booth, M. J., & Wilson, T. (2004). Low-cost, frequency-domain, fluorescence lifetime confocal microscopy. *Journal of Microscopy*, *214*(Pt 1), 36–42.

Breusegem, S. Y., Levi, M., & Barry, N. P. (2006). Fluorescence correlation spectroscopy and fluorescence lifetime imaging microscopy. *Nephron Experimental Nephrology*, *103*(2), e41–e49.

Bugiel, I., König, K., & Wabnitz, H. (1989). Investigation of cell by fluorescence laser scanning microscopy with subnanosecond time resolution. *Lasers in the Life Sciences*, *3*(1), 47–53.

Chang, C.-W., & Mycek, M.-A. (2010a). Precise fluorophore lifetime mapping in live-cell, multi-photon excitation microscopy. *Optics Express*, *18*(8), 8688–8696.

Chang, C.-W., & Mycek, M.-A. (2010b). Enhancing precision in time-domain fluorescence lifetime imaging. *Journal of Biomedical Optics*, *15*(5), 056013.

Chang, C.-W., & Mycek, M.-A. (2012a). Quantitative molecular imaging in living cells via FLIM. In C. D. Geddes (Ed.), *Reviews in fluorescence 2010* (pp. 173–198). New York: Springer.

Chang, C.-W., & Mycek, M.-A. (2012b). Total variation versus wavelet-based methods for image denoising in fluorescence lifetime imaging microscopy. *Journal of Biophotonics*, *5*(5–6), 449–457.

Chang, C.-W., Sud, D., & Mycek, M.-A. (2007). Fluorescence lifetime imaging microscopy. In G. Sluder & D. Wolf (Eds.), *Methods in cell biology*, Vol. 81. London, UK: Elsevier Inc (Chapter 24).

Chang, C.-W., Wu, M., Merajver, S. D., & Mycek, M.-A. (2009). Physiological fluorescence lifetime imaging microscopy improves Förster resonance energy transfer detection in living cells. *Journal of Biomedical Optics*, *14*(6), 060502.

Chen, Y., & Periasamy, A. (2004). Characterization of two-photon excitation fluorescence lifetime imaging microscopy for protein localization. *Microscopy Research and Technique*, *63*(1), 72–80.

Clayton, A. H. A., Hanley, Q. S., & Verveer, P. J. (2004). Graphical representation and multicomponent analysis of single-frequency fluorescence lifetime imaging microscopy data. *Journal of Microscopy*, *213*, 1–5.

Cubeddu, R., Comelli, D., D'Andrea, C., Taroni, P., & Valentini, G. (2002). Time-resolved fluorescence imaging in biology and medicine. *Journal of Physics D: Applied Physics*, *35*, R61–R76.

Demas, J. N. (1983). *Excited state lifetime measurements*. New York: Academic Press.

Digman, M. A., Caiolfa, V. R., Zamai, M., & Gratton, E. (2008). The phasor approach to fluorescence lifetime imaging analysis. *Biophysical Journal*, *94*(2), L14–L16.

Dowling, K., Hyde, S. C. W., Dainty, J. C., French, P. M. W., & Hares, J. D. (1997). 2-D fluorescence lifetime imaging using a time-gated image intensifier. *Optics Communications*, *135*, 27–31.

Ellis, J. D., Lleres, D., Denegri, M., Lamond, A. I., & Caceres, J. F. (2008). Spatial mapping of splicing factor complexes involved in exon and intron definition. *The Journal of Cell Biology*, *181*(6), 921–934, (Research Support, Non-U.S. Gov't).

Förster, T. (1948). Intermolecular energy migration and fluorescence. *Annals of Physics*, *2*, 55–75.

French, T., So, P. T. C., Dong, C. Y., Berland, K. M., & Gratton, E. (1998). Fluorescence lifetime imaging techniques for microscopy. *Methods in Cell Biology*, *56*, 277–304.

Gadella, T. W. J., Jr. (1999). Fluorescence lifetime imaging microscopy (FLIM): Instrumentation and application. In W. T. Masons (Ed.), *Fluorescent and luminescent probes for biological activity* (pp. 467–479). San Diego, CA: Academic Press.

Gerritsen, H. C., Sanders, R., Draaijer, A., & Levine, Y. K. (1997). Fluorescence lifetime imaging of oxygen in living cells. *Journal of Fluorescence*, *7*(1), 11–16.

Ghiggino, K. P., Harris, M. R., & Spizzirri, P. G. (1992). Fluorescence lifetime measurements using a novel fiber-optic laser scanning confocal microscope. *The Review of Scientific Instruments*, *63*(5), 2999–3002.

Heikal, A. A. (2010). Intracellular coenzymes as natural biomarkers for metabolic activities and mitochondrial anomalies. *Biomarkers in Medicine*, *4*(2), 241–263.

Helmchen, F., & Denk, W. (2005). Deep tissue two-photon microscopy. *Nature Methods*, *2*(12), 932–940 (Review).

Hill, N. E. (1969). *Dielectric properties and molecular behaviour*. London/New York: Van Nostrand Reinhold.

Hink, M. A., Bisselin, T., & Visser, A. J. (2002). Imaging protein-protein interactions in living cells. *Plant Molecular Biology*, *50*(6), 871–883.

ISS. Lifetime data of selected fluorophores. http://www.iss.com/resources/fluorophores.html.

Jares-Erijman, E. A., & Jovin, T. M. (2003). FRET imaging. *Nature Biotechnology*, *21*(11), 1387–1395.

Jo, J. A., Fang, Q., & Marcu, L. (2005). Ultrafast method for the analysis of fluorescence lifetime imaging microscopy data based on the laguerre expansion technique. *IEEE Journal of Quantum Electronics*, *11*(4), 835–845.

Kask, P., Palo, K., Ullmann, D., & Gall, K. (1999). Fluorescence-intensity distribution analysis and its application in biomolecular detection technology. *Proceedings of the National Academy of Sciences of the United States of America*, *96*(24), 13756–13761.

Lakowicz, J. R. (2006). *Principles of fluorescence spectroscopy* (3rd ed.). New York: Springer.

Lakowicz, J. R., Szmacinski, H., Nowaczyk, K., & Johnson, M. L. (1992). Fluorescence lifetime imaging of free and protein-bound NADH. *Proceedings of the National Academy of Sciences of the United States of America*, *89*(4), 1271–1275.

Lee, K. C. B., Siegel, J., Webb, S. E. D., Leveque-Fort, S., Cole, M. J., Jones, R., et al. (2001). Application of the stretched exponential function to fluorescence lifetime imaging. *Biophysical Journal*, *81*, 1265–1274.

Lin, H. J., Herman, P., & Lakowicz, J. R. (2003). Fluorescence lifetime-resolved pH imaging of living cells. *Cytometry. Part A*, *52*(2), 77–89.

Lleres, D., James, J., Swift, S., Norman, D. G., & Lamond, A. I. (2009). Quantitative analysis of chromatin compaction in living cells using FLIM-FRET. *The Journal of Cell Biology*, *187*(4), 481–496.

Lloyd, W. R., Chen, L.-C., Kuo, S., Marcelo, C. L., Feinberg, S. E., & Mycek, M.-A. (2012). Fluorescence lifetime imaging microscopy (FLIM) studies of living primary human cells for applications in tissue regeneration. *Proceedings of SPIE*, *8226*, 82260E–82266E.

Lloyd, W. R., Chen, L.-C., & Mycek, M. A. (2013). Fluorescence spectroscopy. In S. P. Morgan, S. J. Matcher, & F. Rose (Eds.), *Optical techniques in regenerative medicine*. Boca Raton, FL: CRC Press.

Lloyd, W. R., Chen, L.-C., Wilson, R. H., & Mycek, M.-A. (2013). Biophotonics: Clinical fluorescence detection. In D. J. Maitland, & J. E. Moore, Jr., (Eds.), *Biomedical technology and devices handbook*. (2nd ed.). Boca Raton, FL: CRC Press.

Lloyd, W., Wilson, R. H., Chang, C.-W., Gillispie, G. D., & Mycek, M.-A. (2010). Instrumentation to rapidly acquire fluorescence wavelength-time matrices of biological tissues. *Biomedical Optics Express*, *1*(2), 574–586.

Marmarelis, V. Z. (1993). Identification of nonlinear biological systems using Laguerre expansions of kernels. *Annals of Biomedical Engineering*, *21*, 573–589.

Mehta, G., Mehta, K., Sud, D., Song, J. W., Bersano-Begey, T., Futai, N., et al. (2007). Quantitative measurement and control of oxygen levels in microfluidic poly(dimethylsiloxane) bioreactors during cell culture. *Biomedical Microdevices*, *9*(2), 123–134.

Ng, T., Squire, A., Hansra, G., Bornancin, F., Prevostel, C., Hanby, A., et al. (1999). Imaging protein kinase C alpha activation in cells. *Science*, *283*(5410), 2085–2089.

Oida, T., Sako, Y., & Kusumi, A. (1993). Fluorescence lifetime imaging microscopy (flimscopy)—Methodology development and application to studies of endosome fusion in single cells. *Biophysical Journal*, *64*(3), 676–685.

Owen, D. M., Auksorius, E., Manning, H. B., Talbot, C. B., de Beule, P. A., Dunsby, C., et al. (2007). Excitation-resolved hyperspectral fluorescence lifetime imaging using a UV-extended supercontinuum source. *Optics Letters*, *32*(23), 3408–3410.

Pande, P., & Jo, J. A. (2011). Automated analysis of fluorescence lifetime imaging microscopy (FLIM) data based on the Laguerre deconvolution method. *IEEE Transactions on Bio-Medical Engineering*, *58*(1), 172–181.

Provenzano, P. P., Eliceiri, K. W., & Keely, P. J. (2009). Multiphoton microscopy and fluorescence lifetime imaging microscopy (FLIM) to monitor metastasis and the tumor microenvironment. *Clinical & Experimental Metastasis*, *26*(4), 357–370.

Redford, G. I., & Clegg, R. M. (2005). Polar plot representation for frequency-domain analysis of fluorescence lifetimes. *Journal of Fluorescence*, *15*(5), 805–815.

Rudolph, W., & Kempe, M. (1997). Trends in optical biomedical imaging. *Journal of Modern Optics*, *44*(9), 1617–1642.

Salthammer, T. (1992). Numerical simulation of pile-up distorted time-correlated single photon counting (TCSPC) data. *Journal of Fluorescence*, *2*(1), 23–27.

Sanders, R., Draaijer, A., Gerritsen, H. C., Houpt, P. M., & Levine, Y. K. (1995). Quantitative pH imaging in cells using confocal fluorescence lifetime imaging microscopy. *Analytical Biochemistry*, *227*(2), 302–308.

Sharman, K. K., Periasamy, A., Ashworth, H., Demas, J. N., & Snow, N. H. (1999). Error analysis of the rapid lifetime determination method for double-exponential decays and new windowing schemes. *Analytical Chemistry*, *71*(5), 947–952.

Skala, M. C., Riching, K. M., Gendron-Fitzpatrick, A., Eickhoff, J., Eliceiri, K. W., White, J. G., et al. (2007). In vivo multiphoton microscopy of NADH and FAD redox states, fluorescence lifetimes, and cellular morphology in precancerous epithelia. *Proceedings of the National Academy of Sciences of the United States of America*, *104*(49), 19494–19499.

Sud, D., Mehta, G., Mehta, K., Linderman, J. J., Takayama, S., & Mycek, M.-A. (2006). Optical imaging in microfluidic bioreactors enables oxygen monitoring for continuous cell culture. *Journal of Biomedical Optics*, *11*, 050504.

Sud, D., & Mycek, M.-A. (2009). Calibration and validation of an optical sensor for intracellular oxygen measurements. *Journal of Biomedical Optics*, *14*(2), 020506.

Sud, D., Zhong, W., Beer, D. G., & Mycek, M.-A. (2006). Time-resolved optical imaging provides a molecular snapshot of altered metabolic function in living human cancer cell models. *Optics Express*, *14*(10), 4412–4426.

Sun, Y., Hatami, N., Yee, M., Phipps, J., Elson, D. S., Gorin, F., et al. (2010). Fluorescence lifetime imaging microscopy for brain tumor image-guided surgery. *Journal of Biomedical Optics*, *15*(5), 056022.

Sun, Y., Phipps, J., Elson, D. S., Stoy, H., Tinling, S., Meier, J., et al. (2009). Fluorescence lifetime imaging microscopy: in vivo application to diagnosis of oral carcinoma. *Optics Letters*, *34*(13), 2081–2083.

Tadrous, P. J. (2000). Methods for imaging the structure and function of living tissues and cells: 2 Fluorescence lifetime imaging. *Journal of Pathology*, *191*(3), 229–234.

Urayama, P. K., & Mycek, M.-A. (2003). Fluorescence lifetime imaging microscopy of endogenous biological fluorescence. In M.-A. Mycek & B. W. Pogue (Eds.), *Handbook of biomedical fluorescence* (pp. 211–236). New York: Marcel Dekker, Inc.

Urayama, P. K., Zhong, W., Beamish, J. A., Minn, F. K., Sloboda, R. D., Dragnev, K. H., et al. (2003). A UV-visible fluorescence lifetime imaging microscope for laser-based biological sensing with picosecond resolution. *Applied Physics B-Lasers Optics*, *76*(5), 483–496.

van Munster, E. B., & Gadella, T. W. J. (2005). Fluorescence lifetime imaging microscopy (FLIM). *Advances in Biochemical Engineering/Biotechnology*, *95*, 143–175.

Vermeer, J. E., van Munster, E. B., Vischer, N. O., & Gadella, T. W., Jr. (2004). Probing plasma membrane microdomains in cowpea protoplasts using lipidated GFP-fusion proteins and multimode FRET microscopy. *Journal of Microscopy*, *214*(Pt 2), 190–200.

Wahl, M., Koberling, F., Patting, M., Rahn, H., & Erdmann, R. (2004). Time-resolved confocal fluorescence imaging and spectrocopy system with single molecule sensitivity and sub-micrometer resolution. *Current Pharmaceutical Biotechnology*, *5*(3), 299–308.

Wallrabe, H., & Periasamy, A. (2005). Imaging protein molecules using FRET and FLIM microscopy. *Current Opinion in Biotechnology*, *16*(1), 19–27.

Wang, X. F., Periasamy, A., Herman, B., & Coleman, D. (1992). Fluorescence lifetime imaging microscopy (FLIM): Instrumentation and applications. *Critical Reviews in Analytical Chemistry*, *23*(5), 369–395.

Wang, X. F., Uchida, T., Coleman, D. M., & Minami, S. (1991). A two-dimensional fluorescence lifetime imaging system using a gated image intensifier. *Applied Spectroscopy*, *45*(3), 360–366.

Zhong, W., Urayama, P., & Mycek, M.-A. (2003). Imaging fluorescence lifetime modulation of a ruthenium-based dye in living cells: The potential for oxygen sensing. *Journal of Physics D: Applied Physics*, *36*(14), 1689–1695.

Zhong, W., Wu, M., Chang, C. W., Merrick, K. A., Merajver, S. D., & Mycek, M. A. (2007). Picosecond-resolution fluorescence lifetime imaging microscopy: A useful tool for sensing molecular interactions in vivo via FRET. *Optics Express*, *15*(26), 18220–18235.

Zipfel, W. R., Williams, R. M., Christie, R., Nikitin, A. Y., Hyman, B. T., & Webb, W. W. (2003). Live tissue intrinsic emission microscopy using multiphoton-excited native fluorescence and second harmonic generation. *Proceedings of the National Academy of Sciences of the United States of America*, *100*(12), 7075–7080.